Review of Scientific Instruments

RESEARCH ARTICLE | JANUARY 28 2026

A liquid-phase high-order harmonic generation apparatus for investigating ultrafast dynamics in liquids FREE

Wenchao Zhao ; Zepeng Qian ; Yuanjie Pan ; Jinkai Zhang ; Menglong Zhao ; Gefei Li ; Tien-Dat Tran ; Tran Trung Luu ; Pengju Zhang

Rev. Sci. Instrum. 97, 013005 (2026)
https://doi.org/10.1063/5.0278967

AIP Publishing

Review of Scientific Instruments ARTICLE pubs.aip.org/aip/rsi

A liquid-phase high-order harmonic generation apparatus for investigating ultrafast dynamics in liquids

Cite as: Rev. Sci. Instrum. 97, 013005 (2026); doi: 10.1063/5.0278967
Submitted: 5 May 2025 • Accepted: 2 January 2026 •
Published Online: 28 January 2026

Wenchao Zhao,[1,a] Zepeng Qian,[2,b),c)] Yuanjie Pan,[1,b)] Jinkai Zhang,[3,c)] Menglong Zhao,[4,a),c)] Gefei Li,[1,b)] Tien-Dat Tran,[5] Tran Trung Luu,[5] and Pengju Zhang[1,b),d)]

AFFILIATIONS

[1] Institute of Physics, Chinese Academy of Sciences, Beijing 100190, China
[2] School of Optoelectronic Science and Engineering, South China Normal University, Guangzhou 510631, China
[3] Institute of Theoretical Physics, State Key Laboratory of Quantum Optics and Quantum Optics Devices, Taiyuan 030006, China
[4] School of Mechanical and Automotive Engineering, South China University of Technology, Guangzhou 510641, China
[5] Department of Physics, University of Hong Kong, Hong Kong SAR 999077, China

[a)] **Also at:** Songshan Lake Materials Laboratory, Dongguan 523808, China.
[b)] **Also at:** School of Physical Sciences, University of Chinese Academy of Sciences, Beijing 100190, China.
[c)] **Also at:** Institute of Physics, Chinese Academy of Sciences, Beijing 100190, China.
[d)] **Author to whom correspondence should be addressed:** pengju.zhang@iphy.ac.cn

ABSTRACT

To investigate the electronic-dominated ultrafast dynamics in liquids, we built a liquid high-order harmonic generation (HHG) apparatus, which consists of an ultrafast laser system, a liquid flatjet system, and an extreme ultraviolet (EUV) spectrometer. The performance of this apparatus was systematically examined through the generation of HHG spectra from 99.7% isopropanol [$(CH_3)_2CHOH$], 99.7% ethanol (CH_3CH_2OH), and liquid water (H_2O). A negligible contribution from the gas-phase was verified by a direct comparison between the liquid-phase and gas-phase under an optimal configuration. Under the current experimental conditions, the measured high-order harmonic spectra (HHS) exhibited a distinct maximum photon energy of 20 eV, with intensity decreasing as the harmonic order increased. Our two-band model based on the semiconductor Bloch equations suggests that HHSs from liquids reach saturation very quickly. Moreover, we measured the time-dependent HHS of liquid isopropanol [$(CH_3)_2CHOH$] using a non-collinear 800 nm pump–probe Mach–Zehnder interferometer. These preliminary results demonstrate the operational capability of liquid-based HHG spectroscopy and highlight its potential for probing ultrafast electron dynamics and molecular properties in liquids.

I. INTRODUCTION

The advent of attosecond laser pulses via high-harmonic generation (HHG)[1,2] has undoubtedly revolutionized the field of light–matter interactions and significantly advanced attosecond science, particularly in the study of structural and electronic dynamics in atoms,[3,4] molecules,[5–7] liquids,[8] and solids.[9,10] Over the past few decades, HHG has been experimentally demonstrated in all phases of matter: gases, solids, and liquids. In the gas phase, where HHG was first discovered,[11] it has been extensively researched and is well understood. The high-order harmonic spectrum (HHS) from the gas-phase medium,[1,12] well-described by a three-step model[13] and considered as a self-probe approach, has been utilized to study the electronic dynamics in atoms and molecules. Furthermore, the gas-phase HHG has evolved into a widely used laboratory-based attosecond laser source of extreme ultraviolet (EUV) radiation, enabling real-time studies of structural and electronic dynamics in molecules, solutions, and solids. However, the low density of gases results in a low photon flux, which limits the efficiency of experiments. In contrast, solids have the advantage of having high density and can

be integrated, making them another important source of high harmonics. Since the early pioneering work,[14–16] the solid-phase HHG has developed very rapidly, leading to impressive advancements.[17,18] Meanwhile, the principal microscopic mechanisms associated with solid-phase HHG have been further refined,[19] although consensus on several aspects is still forming. However, the practicality of solids as attosecond light sources is constrained by their lack of self-renewal capability, which makes them highly susceptible to cumulative laser-induced damage and, thus, prevents sustained long-term operation.

In recent years, liquid-phase HHG has received considerable attention because liquids have the advantages of both the self-renewal capability akin to gases and the high density of solids and because the vast majority of chemical reactions occur in the liquid or hydrated phase. In contrast to gas and solid phases, measurements of liquid-phase HHG remain quite scarce. Since 2003, several experiments have been performed on HHG associated with liquid droplets.[20–22] Incoherent EUV HHG was observed at the density of natural water, while coherent HHG was detected only after the droplets expanded to high pressure gas.[20–22] Moreover, the thin liquid film was also utilized as a self-refreshing target for generating high-order harmonics. In 2003, Tauber *et al.*[23] developed a wire-guided, gravity-driven jet apparatus capable of producing stable liquid films. However, this setup was not suitable for vacuum environments, as the liquid film would rapidly condense under low pressure. In 2009, DiChiara *et al.*[24] adapted this jet apparatus to generate a 150-μm-thick liquid film in an atmospheric environment as an HHG experimental target. While they successfully observed harmonic signals in the visible range, harmonics in the EUV region were not detected. This limitation was attributed to strong absorption of high-energy photons by both the ambient air and the relatively thick liquid film, which suppressed the generation and detection of higher-order harmonics. To access higher-order harmonics with greater photon energies, an ultra-thin liquid film operated under vacuum conditions is necessary. In the last decade, the development of ultrathin liquid flatjet technology[25–32] has enabled the fabrication of μm-scale ultrathin liquid films under vacuum conditions, significantly advancing experimental research in liquid HHG. More recently, Luu *et al.*[33] employed liquid flatjet technology to create an ultrathin liquid flatjet with a thickness of ~2 μm, leading to the experimental discovery of HHG radiation in the EUV region. They found that the HHSs of H_2O and alcohols exhibit odd-only HHG, with cutoffs around 20 eV. In addition, the intensities of the HHSs of the alcohols decrease monotonically with photon energy, while the HHS of H_2O shows a plateau followed by a steep decline toward the cutoff. Luu *et al.*[33] treated the liquid as a large-bandgap semiconductor and derived a highly simplified model band structure based on the density of states of the liquid. By solving the semiconductor Bloch equation, they theoretically predicted a harmonic spectrum consistent with experimental results. Their findings indicated that the harmonic generation from liquids is sensitive to the electronic structure of the liquids, particularly the properties of the conduction band and the bandgap.

Following this, a series of liquid-phase HHG studies were conducted,[34–42] collectively demonstrating the potential of liquids as a bright source of high-order harmonics and paving the way for further advancements in liquid-phase HHG and HHS. In these studies, a consistent conclusion is proposed: liquid-phase HHG provides a means to probe ultrafast electron dynamics in liquids, including electron mean free paths[38,39] and scattering processes,[41] which are crucial for understanding radiation-induced damage in biological tissues. However, notable discrepancies exist among experimental observations. In particular, some work reports harmonic energies of liquids extending only up to about 20 eV,[33,36,38,39] with cutoff energies showing independence on driving laser wavelength or pulse duration.[38,39] In contrast, Alexander *et al.*[41] reported that, when the laser intensity is below the damage threshold of the liquid, the harmonic energy driven by few-cycle lasers can reach a maximum around 50 eV and exhibits a dependence on both the laser intensity and the pulse duration. Conversely, when the laser intensity exceeds the damage threshold, a plasma mirror forms on the front surface of the liquid flatjet, reflecting a portion of the incident light. This reflection reduces the effective intensity within the liquid, leading to a suppression of harmonic yield and a lowering of the harmonic energy. *Ab initio* quantum dynamics simulations by Xu *et al.*[43] support this picture, indicating that plasma generation in liquid suppresses the intensity and the energy of high-order harmonics. Recent work by Kim *et al.*[40] and Cavagna *et al.*[44] demonstrated that the liquid plasma mirror can also generate the high-order harmonics in both the coherent wake emission and relativistic oscillating mirror regimes, suggesting additional pathways to HHG in liquid systems. Moreover, Yang *et al.*[42] revealed an additional mechanism whereby resonant infrared excitation drives ultrafast heating of the liquid, leading to a pronounced and persistent enhancement of harmonic yield. These divergent results underscore the complexity of laser–liquid interactions and emphasize the need for more systematic, controlled studies to disentangle the roles of intensity, pulse duration, damage threshold, and plasma formation in liquid-phase HHG and to establish a coherent framework for interpreting harmonics in liquid media.

As a highly disordered condensed phase, liquids cannot be easily treated as isolated molecules, as is the case with gases, nor can they be characterized by a highly periodic lattice structure, as seen in solids. Consequently, the mechanisms and analytic approaches developed for gas and solid media cannot be directly applied to liquids. Currently, there is a lack of an appropriate and feasible model to describe the mechanism of light–matter interaction in liquids, resulting in slow progress in research related to liquid HHG, which requires further exploration. Because of its strong capability to probe electronic and nuclear dynamics in liquid-phase environments, we developed a liquid HHG apparatus.

In this work, HHG experiments were conducted using various liquid systems as samples to obtain their HHSs, which are consistent with previous HHG studies,[33,38] thereby confirming the reliability and performance of this liquid-phase HHG setup. Building on our liquid-HHG setup, we integrated a pump–probe device to enable time-resolved HHG spectroscopy of liquid samples. This capability allows us to investigate fundamental ultrafast processes, including solvation dynamics, charge transfer, and bond breaking/formation. Furthermore, the setup shares an identical configuration for transient absorption spectroscopy in liquids,[45,46] creating a dual-function apparatus. This platform provides a comprehensive tool for studying light–matter interactions in liquids across diverse timescales and energy regimes.

II. EXPERIMENTAL SETUP

The experimental setup is schematically depicted in Fig. 1(a). The main components of the apparatus include a laser system, a liquid flatjet system within the reaction chamber, and an EUV spectrometer within the detection chamber. The laser system can generate laser pulses with a center wavelength of 800 nm, a full width at half maximum (FWHM) of 33 nm, a pulse width of 45 fs, a repetition frequency of 1 kHz, and a pulse energy of 200 μJ. After collimation and focusing, the laser pulses enter the reaction chamber through a 2-mm-thick ultraviolet-fused silica glass window, where they interact with an ultrathin liquid flatjet produced by the collision between two round liquid micro-jets, generating high-order harmonics in the EUV wavelength range. Figure 1(b) shows a photograph of a laser pulse interacting with a liquid flatjet. The interaction region was positioned at the center of the flatjet. The laser was focused to a spot diameter of ~260 μm, as measured by a beam profiling camera. This spot size yields a peak electric field strength of 0.85 V/Å. The generated harmonics propagate through a differential pinhole that connects the interaction and detection chambers. These harmonics are then recorded by the EUV spectrometer to obtain the liquid HHS. The side and top views of the experimental setup are given in Figs. 1(c) and 1(d), respectively, providing a detailed workflow of the spectrometer along with technical information.

A. Liquid flatjet system

An ultrathin liquid flatjet that remains stable in both diameter and thickness for up to several hours is essential for successfully executing the HHG experiment. To produce the required liquid flatjet, we constructed a liquid flatjet apparatus based on the method developed by Ekimova *et al.*[26] A liquid sample is pumped into the vacuum chamber at room temperature using a high-performance liquid chromatography (HPLC) pump purchased from WATREX Prague (Model: P102). The pump operates at flow rates between 0.1 and 10 ml/min with a stability better than ±0.5%. A multi-channel switching valve is fitted upstream of the HPLC pump to facilitate sample switching. The liquid flow is then split into two streams, each entering the vacuum chamber through separate capillary arrays

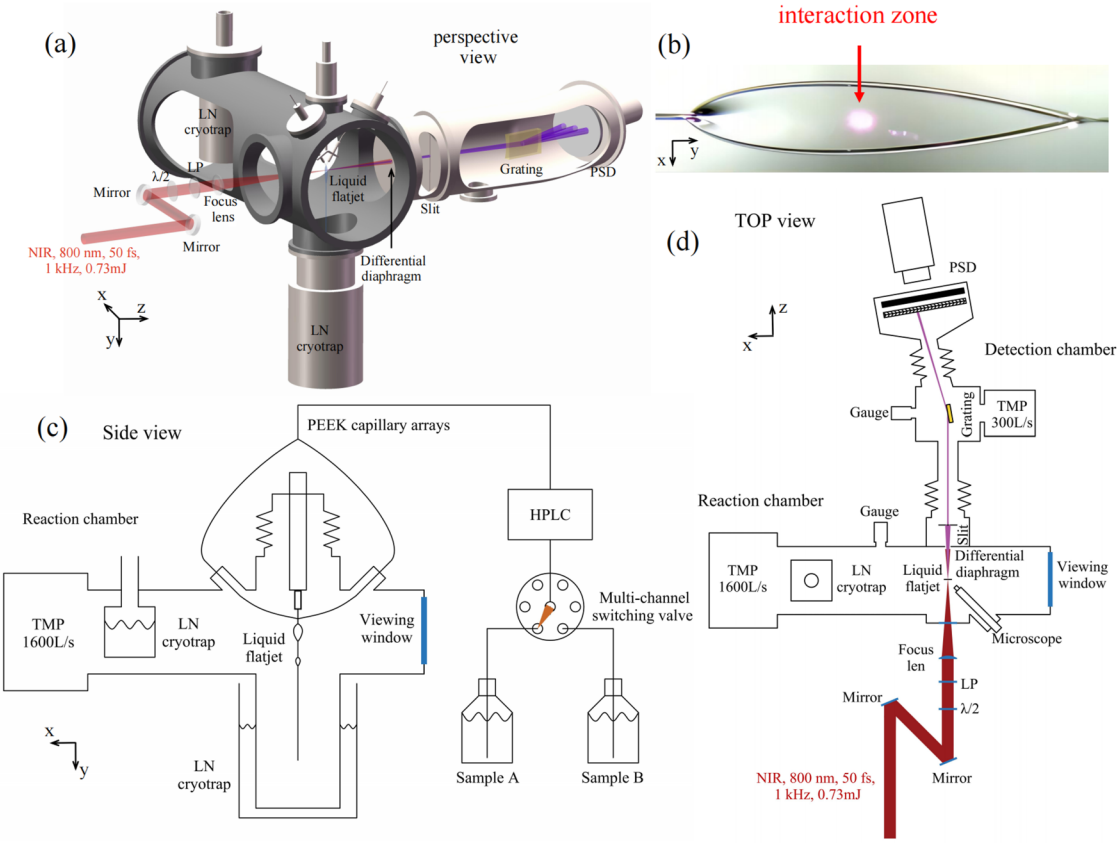

FIG. 1. Liquid HHG spectrometer. (a) Schematic depiction of the experimental setup. Laser pulses (800 nm, 1 kHz, 50 fs, and 0.73 mJ) are focused onto a liquid flatjet to generate high-order harmonics. The generated high-order harmonics pass through a slit into the extreme-ultraviolet (EUV) spectrometer that disperses and records the different harmonic orders. (b) Photograph of the laser pulse interacting with the liquid flatjet. [(c) and (d)] Side and top views of the experimental setup. LP: linear polarization; LN_2: liquid nitrogen; PSD: position-sensitive detector, which is equipped with a pair of micro-channel plates, a phosphor screen, and a charge-coupled device camera.; TMP: turbomolecular pump; PEEK: poly-ether ether ketone; HPLC: high-performance liquid chromatography.

and exiting through identical cylindrical glass nozzles. The capillary arrays are made of poly-ether ether ketone with varying inner diameters arranged in increasing order to ensure a more uniform flow. When two individual laminar liquid streams collide at a specific angle that is not equal to 180°(66° in this work), their opposing horizontal momentum components mutually cancel. This causes the incompressible liquid to expand radially within the collision plane, thereby producing a stable planar liquid sheet through progressive thinning and flattening in this direction. Surface tension in the liquid then overcomes radial diffusion, causing the liquid jet to reconverge and resulting in the formation of a liquid flatjet shaped like a sharp leaf, characterized by a thin center and relatively thick liquid edges. In this work, water (H_2O), 99.7% ethanol (CH_3CH_2OH), and 99.7% isopropanol [$(CH_3)_2CHOH$] were chosen as liquid samples due to their viscosity and vapor pressure, which support the formation of optimal flatjets.

To achieve the thinnest possible flatjet, the liquid must be produced with a minimal volume, requiring nozzle dimensions of tens of μm. In this work, the diameter of the nozzles used is about 55 μm, measured using a microscope. It was found that the liquid flatjet remains stable only within a specific flow rate range. In our setup, we optimized the flow rate between 3 and 5 ml/min to achieve a stable liquid flatjet. Flow rates above this range cause the liquid flatjet to collapse, while rates below this range fail to generate the desired liquid flatjet. The liquid flatjet apparatus is mounted on a precision four-axis (XYZR) manipulator for finer adjustment of the azimuth and three-dimensional position of the liquid flatjet relative to the laser beam. In addition, a microscope is positioned in the reaction chamber to monitor the quality of the liquid flatjet in real time. Long-term monitoring confirmed that the flatjet can remain structurally stable for several hours.[26,29,30] When the liquid flatjet enters the vacuum at room temperature, the evaporation of the liquid removes heat, causing the flatjet temperature to drop. The magnitude of the drop depends on the evaporation rate of the liquid and the surface area of the flatjet, leading to sample-dependent cooling. Measurements show that liquid H_2O experiences a temperature drop on the order of ~20 °C,[26,30] whereas a larger drop of ~45 °C is observed for liquids CH_3CH_2OH and $(CH_3)_2CHOH$.[29,30,38]

B. EUV spectrometer

The EUV spectrometer, used to detect and analyze the high-order harmonic emission, consists of an entrance slit, a commercial diffraction grating, and a position-sensitive detector (PSD). The commercial diffraction grating, purchased from Shimadzu, has a groove density of 500 lines/mm, an incidence angle of 10°, and a sensitive wavelength range of 27–135 nm. The PSD is equipped with a pair of micro-channel plates, a phosphor screen, and a charge-coupled device camera. The generated high-order harmonics pass through the slit and are directed toward the diffraction grating, where they are dispersed into various diffraction angles based on their orders. These dispersed harmonics are then detected and read out by the PSD.

The harmonics of different orders diffract at distinct angles and are spatially separated on the PSD. The harmonic orders can, thus, be determined by analyzing their positions and separation distances, allowing for calibration of the EUV spectrometer. In this work, the harmonic orders were identified based on their spacing, as shown in Fig. 2. Figure 2(a) illustrates the optical configuration of the EUV spectrometer, including the incident angle α of HHG and the diffraction angles β_i corresponding to different harmonic orders. From these parameters, the harmonic spacings l_i and their ratios $l_i : l_j$ were derived. Figure 2(b) presents a raw PSD image of harmonics generated in a gaseous CH_3CH_2OH, showing fifth-harmonic components labeled A through E. The measured ratios of the spacings between adjacent harmonics are summarized in the table accompanying Fig. 2(b) and show close agreement with the expected values. This agreement enables clear assignment of harmonic orders and facilitates accurate calibration of the spectrometer. The energy resolution δE/E of this EUV spectrometer is determined from the FWHM (δE) of the harmonic peaks, yielding δE/E ≈ 2%. Furthermore, the system exhibits a dynamic range ~10 000:1 and

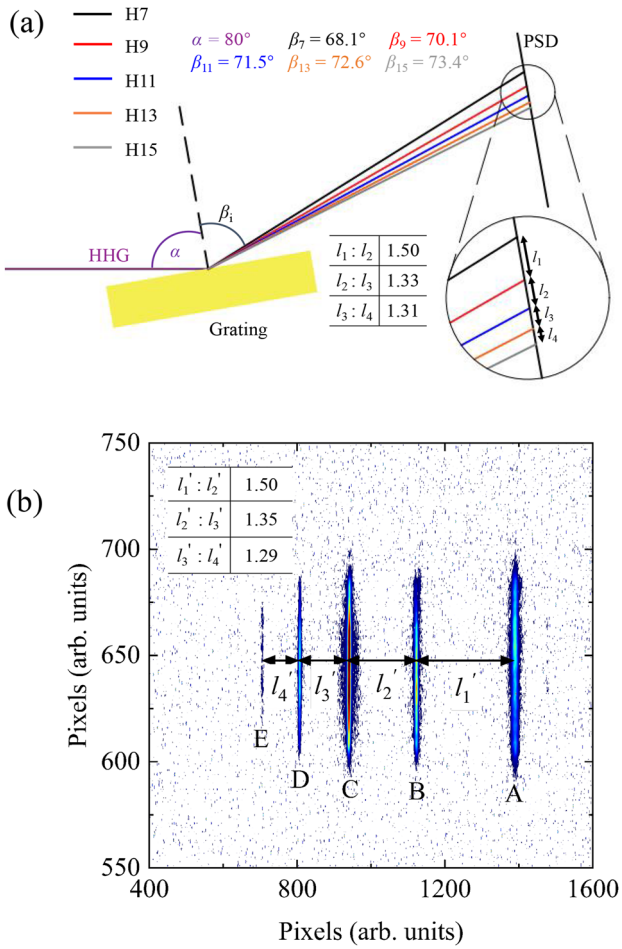

FIG. 2. Calibration of the EUV spectrometer using harmonics generated in gaseous CH_3CH_2OH. (a) Optical configuration of the EUV spectrometer. α and β_i are incident angle of HHG and the diffracted angles of different harmonic orders. l_i and $l_i : l_j$ are the spacings between adjacent harmonics and their ratios derived by the optical configuration. (b) Raw PSD image of harmonics generated in a gaseous CH_3CH_2OH medium, showing fifth-harmonic components labeled A through E. l_i' and $l_i' : l_j'$ are ratios of the spacings between adjacent harmonics and their ratios.

a signal-to-noise ratio of ~200:1, ensuring reliable detection and quantification of harmonic signals across a wide intensity range.

C. Vacuum chambers

Since the working pressure of the reaction chamber is 10^2–10^3 times higher than that of the detection chamber, the two chambers are separated by a differential diaphragm with an inner diameter of 2 mm to minimize their interaction. An Edwards turbomolecular pump with a pumping speed of 1600 l/s and an Edwards rotary mechanical pump with a pumping speed of 35 m^3/h are employed to evacuate the reaction chamber, achieving an ultimate vacuum of 5×10^{-7} mbar. In the detection chamber, a Leybold turbomolecular pump with a pumping speed of 300 l/s, along with a Leybold rotary mechanical pump with a pumping speed of 30 m^3/h, is used to achieve an ultimate vacuum of 8×10^{-8} mbar.

Liquid samples with high vapor pressures evaporate rapidly upon entering the vacuum chamber, raising the pressure to ~10^{-1} mbar in the reaction chamber and to 10^{-3} mbar in the detection chamber. These pressures are too high for the EUV spectrometer with a normal operating pressure of around 10^{-6} mbar. To mitigate this issue, two liquid nitrogen (LN_2) cryotraps were installed in the reaction chamber to reduce the evaporation rate of the liquid target and obtain a lower operating air pressure. With the implementation of these LN_2 cryotraps, the operating pressures stabilize at 10^{-3} mbar in the reaction chamber and 10^{-6} mbar in the reaction chamber. The pressure in both chambers exhibits no significant fluctuation over 30 min following the filling of the cryotraps with liquid nitrogen, demonstrating high pressure stability within the system. By periodically replenishing the liquid nitrogen, pressure stability can be maintained for extended periods exceeding ten hours.

III. FLATJET CHARACTERIZATION UNDER ATMOSPHERIC CONDITIONS

To evaluate the quality and stability of the liquid flatjet, it was generated under atmospheric conditions and monitored for extended periods, revealing stability for up to tens of hours. A representative image of the liquid flatjet in Fig. 3(a) demonstrates the surface quality and integrity of the liquid flatjet, and its size, defined as width and length, can be extracted from this image. The sizes of the flatjets are influenced by the flow rate and the type of liquid, enabling the production of flatjets with varying sizes by adjusting these parameters. Figures 3(b)–3(d) depict the relationship between flatjet size and flow rate for different liquids: $(CH_3)_2CHOH$, CH_3CH_2OH, and H_2O. The results indicate that the size of the liquid flatjet increases with the flow rate, consistent with the experimental result of Ekimova *et al.*[26]

Thin-film interferometry is a valuable tool for measuring the thickness of the liquid flatjet. The setup, illustrated in Fig. 4(a), consists of a halogen light source, two focus lenses, a fiber-coupled spectrometer, and an ultrathin liquid flatjet to be measured. Continuous light with wavelengths from 450 to 950 nm is emitted from the light source, focused by the convex lenses into a spot with a diameter of 200 μm, and directed at the liquid flatjet at a specific incident angle θ. Light reflected from the front and back surfaces of the liquid flatjet was subsequently focused onto a fiber-coupled spectrometer and recorded. The thickness of the film creates phase differences between the reflected light, resulting in interference fringes in the

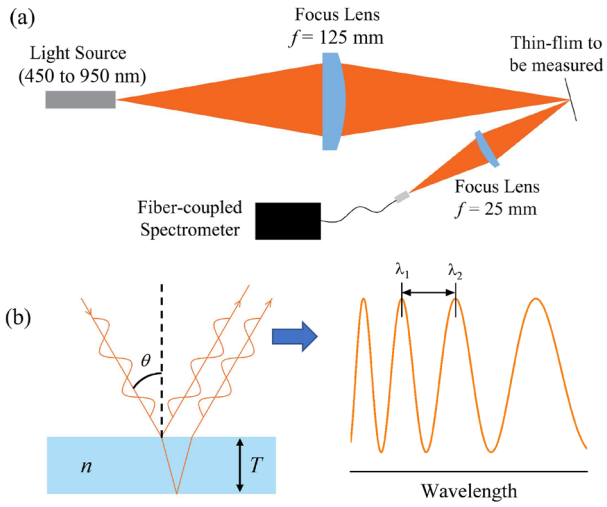

FIG. 4. (a) Schematic diagram and (b) principle diagram of a thin-film interferometer. θ is the incident angle of the light, while n and T are the refractive index and thickness of the thin-film.

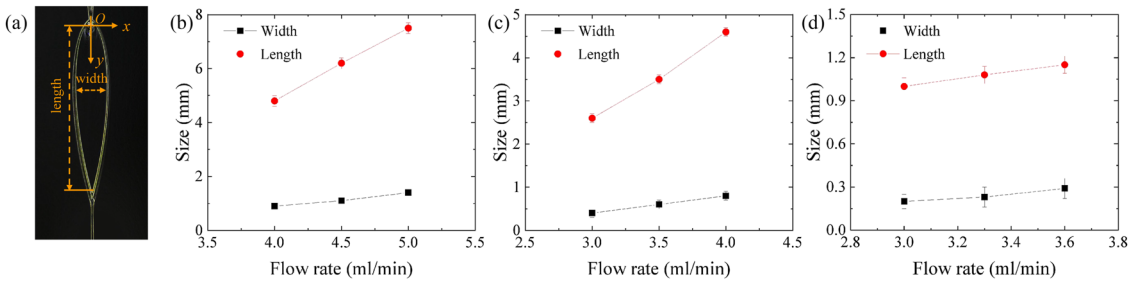

FIG. 3. Size of the liquid flatjet. (a) Photo of the liquid flatjet and the definition of the size of the flatjet. The length is defined as the distance between the upper and lower vertices, and the width is defined as the length of the plane jet at its widest position. The origin of the coordinate axes is defined as the upper vertex of the flatjet, the y axis is defined as the centerline of the liquid flatjet, and the x axis is orthogonal to the y axis in this plane. [(b)–(d)] Flatjet size as a function of flow rate for $(CH_3)_2CHOH$, CH_3CH_2OH, and H_2O.

spectrum, as shown in Fig. 4(b). The thickness of the liquid flatjet can be obtained from the wavelengths of adjacent peaks in those fringes. Figure 5(a) displays the interference spectrum of the $(CH_3)_2CHOH$ flatjet at a flow rate of 5 ml/min, measured at y = 3.5 mm. The average thickness, calculated from the spacing between all adjacent peaks, was determined to be 1.8 ± 0.1 μm. By scanning the position of the liquid flatjet, the thickness can be measured at various locations. The thickness profiles along the y axis of the flatjets for each liquid sample at different flow rates are presented in Figs. 5(b)–5(d). Each data point was acquired over a total measurement time of ~30 min, conducted in three sessions spaced 24 h apart, demonstrating stability and reproducibility with a precision better than 0.2 μm.

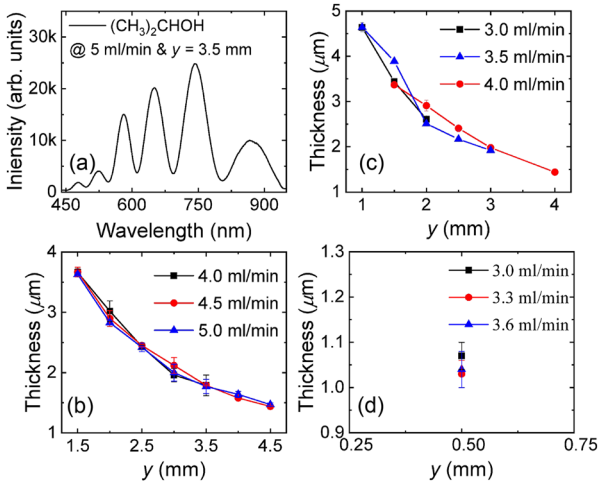

FIG. 5. Thickness of liquid flatjets measured by thin-film interferometry. (a) Interference spectrum of the $(CH_3)_2CHOH$ flatjet at a flow rate of 5 ml/min, measured at y = 3.5 mm. [(b)–(d)] Thickness profiles along the y axis of the flatjets for $(CH_3)_2CHOH$, CH_3CH_2OH, and H_2O as a function of the flow rates. The error bars represent the standard deviation from three repeated measurements.

Due to the small size of the H_2O flatjet, only a single-point thickness measurement was feasible, taken at y = 0.5 mm, yielding a thickness of 1.1 ± 0.1 μm. In contrast, multi-point thickness measurements were performed for the CH_3CH_2OH and $(CH_3)_2CHOH$ flatjets, revealing thicknesses ranging from 1 to 5 μm. Consistent with previous studies,[25–28] the thickness of the flatjets decreases monotonically along the y axis. Notably, the thickness at specific locations was not sensitive to the flow rate under current experimental conditions. Due to the limitations of the experimental conditions, we did not measure the thickness of the liquid flatjet in vacuum. However, the results of Ekimova *et al.*[26] indicate that the difference in the thickness of the liquid flatjet between vacuum and atmospheric conditions is only 5%. Therefore, the thickness of the liquid flatjet measured under atmospheric conditions can be considered equivalent to that in vacuum.

IV. RESULTS AND DISCUSSION

Figure 6(a) presents the HHS of the liquid $(CH_3)_2CHOH$ measured using the PSD, where the spectra were acquired from the center of the flatjet with its thickness estimated as ~1.7 μm. The spectrum clearly resolves four distinct odd harmonics: the 7th (H7), 9th (H9), 11th (H11), and 13th (H13). Among these, H7, H9, and H11 are comparatively strong, while H13 is relatively weak. The absence of observed even-order harmonics indicates that contributions from the surface of the liquid flatjet are negligible. The vertical integration of the PSD image from Fig. 6(a) yields the HHS shown in Fig. 6(b), which displays a generally decreasing signal trend with increasing harmonic order beyond H7. The HHSs of liquid CH_3CH_2OH and H_2O are plotted in Figs. 6(c)–6(f), respectively. Similar to $(CH_3)_2CHOH$, both liquids also produce four odd harmonics (H7, H9, H11, and H13), with signal intensities decreasing beyond H7. The behaviors of HHS for $(CH_3)_2CHOH$ and CH_3CH_2OH are qualitatively consistent with previous reports in liquid-phase HHG[33,38,39] and may be related to the fact that the photon energy of H7 is near the reported cutoff energies of ~11 eV for $(CH_3)_2CHOH$[39] and CH_3CH_2OH,[38] beyond which the

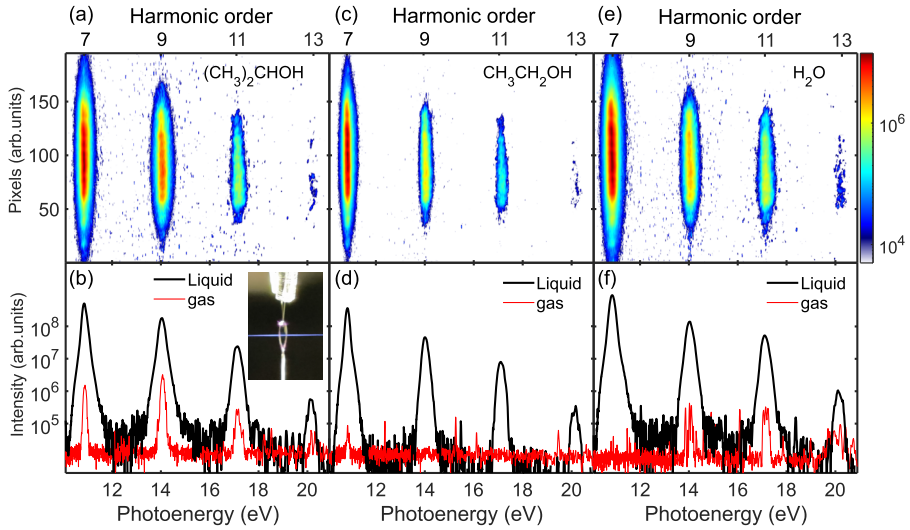

FIG. 6. High-harmonic spectra from liquid samples. (a) Spatio-spectrally resolved and (b) vertically integrated HHSs from the liquid $(CH_3)_2CHOH$ driven by an 800 nm laser. Inset in (b): Experimental configuration for isolating the gas-phase harmonic emission, with the liquid flatjet aligned parallel to the laser propagation axis and placed adjacent to the beam. [(c)–(f)] Typical spatio-spectrally resolved HHSs (top) and their vertical integration (bottom) of HHSs obtained from liquid CH_3CH_2OH and H_2O. For comparison, HHSs from gaseous samples are also shown. Noted that the HHS of gaseous H_2O was measured at 1.27 V/Å, as no harmonics were detected at 0.85 V/Å.

conversion efficiency decreases markedly. However, the HHS of H_2O does not exhibit the plateau reported in previous studies,[33,38] which may be attributed to the substantially lower laser field strength employed in this work (0.85 V/Å) compared to those used in earlier experiments (1.5[33] and 4.2 V/Å[39]), and which is insufficient to drive the higher-order harmonic generation responsible for such a plateau feature.

Due to the evaporation of liquid samples in vacuum, high-density vapors with a number density ranging from 10^{16} to 10^{18}/cm^3 are present near the liquid flatjet.[29] To quantitatively evaluate the potential contribution of this vaporized material to the detected harmonic signal, a dedicated control experiment was performed. The liquid jet was rotated and aligned parallel to the direction of laser propagation, positioning it immediately adjacent to the focused beam as illustrated in the inset of Fig. 6(b). In this configuration, the laser interacts primarily with gas-phase species evaporated from the flatjet over an extended region several millimeters in length, while minimizing direct interaction with the bulk liquid. Under otherwise identical experimental conditions, the integrated harmonic signal from this vapor-phase measurement was found to be over two or three orders of magnitude weaker than that generated from the standard perpendicular interaction with the liquid jet, as shown in Figs. 6(b), 6(d), and 6(f). It should be noted that the HHS of gaseous H_2O was measured under a field strength of 1.27 V/Å, as no harmonics were detected under a field strength of 0.85V/Å. This stark contrast in signal strength strongly indicates that the high-harmonic generation observed under identical experimental conditions originates primarily from the bulk liquid phase and that the contribution from the surrounding vapor is negligible. Although the liquid–laser interaction length is orders of magnitude shorter than that typically achieved in gas-phase targets, the dramatically higher HHG yield observed from the liquid is consistent with its greater density and suggests that liquid targets hold significant promise for achieving high photon flux. It should be noted that although the pronounced enhancement of the harmonic signal from the liquid target compared to gas-phase targets clearly indicates greatly improved efficiency under the present conditions, a definitive comparison of absolute photon flux will require future calibrated measurements against an optimized gas jet. Nevertheless, this result demonstrates the potential of liquid-phase targets as intense EUV sources.

To evaluate the influence of laser field strength on HHG in liquids, we took measurements under a broad range of field strengths. The harmonic intensities of the liquid $(CH_3)_2CHOH$, CH_3CH_2OH, and H_2O as a function of the field strengths are shown in Figs. 7(a)–7(c), and the harmonic intensities exhibit a clear dependence on the field strengths. At the lowest field strength of 0.21 V/Å, only the H7 and H9 harmonics can be observed. With increasing field strength, additional harmonics emerge, culminating in four clearly resolved orders, from H7 to H13. The maximum detectable photon energy shows a strong dependence on the laser field strength, reaching about 20 eV under the highest fields applied in this study. Although this result is consistent with some previous reports,[33,38,39] it is noteworthy that higher cutoffs have been observed under different experimental configurations.[41,47] By improving the signal-to-noise ratio of the detection system, Mondal *et al.*[47] successfully detected harmonic signals with photon energies beyond 20 eV, despite their extremely low intensities, while Alexander *et al.*[41] reported harmonics up to 50 eV driven by few-cycle laser sources with durations of 1.8 optical cycles, which is significantly shorter than our durations of over ten optical cycles. These observed discrepancies do not contradict our results but rather reflect fundamental differences under experimental conditions—particularly in laser pulse duration and detection sensitivity. Consequently, future work will focus on systematically investigating the influence of pulse duration on high-harmonic generation in liquids, alongside improving the sensitivity, noise performance, and stability of our detection system. Such efforts are essential both for accessing weak high-harmonic signals and for enabling a more comprehensive exploration of the physical mechanisms underlying liquid-phase HHG. Furthermore, a clear and consistent saturation trend is observed across all harmonic orders and sample types: as the laser field strength increases, the harmonic intensity initially rises rapidly, then exhibits a slowed growth rate, and eventually approaches saturation at higher field levels. Notably, the intensity growth rate varies considerably across different harmonic orders and samples, indicating a field-dependent redistribution of harmonic intensity ratios.

V. PROPAGATION EFFECT AND BAND STRUCTURE

Considering the absorption and dispersion effects caused by the liquid flatjet, it is crucial to clarify that the characteristics observed in the experimental results derive entirely from the intrinsic properties of the liquid flatjet, rather than from the aforementioned effects or being overshadowed by such effects to the extent that their intrinsic properties are obscured. On the one hand, we solved the first order Maxwell's equations combined with Semiconductor Bloch Equations (SBEs) to capture both the absorption and dispersion effects on HHG spectra transmitted through the flatjet. For simplicity, we simulated the HHSs from liquid H_2O and consider the refractive index of liquid water. The liquid H_2O is

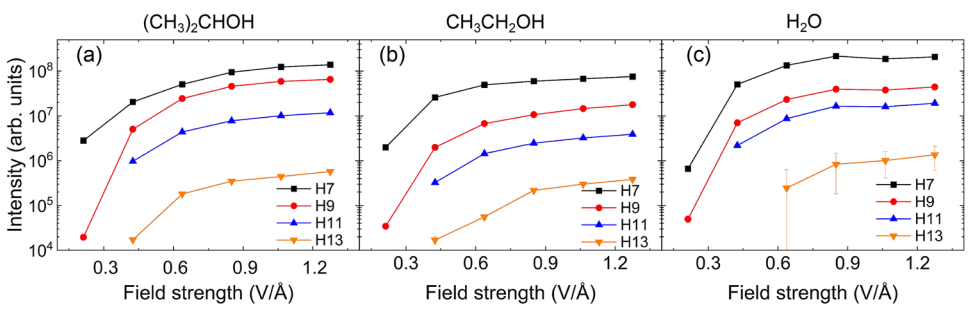

FIG. 7. [(a)–(c)] Harmonic intensities of the liquid $(CH_3)_2CHOH$, CH_3CH_2OH, and H_2O as a function of the field strengths. The error bars represent the standard deviation from five repeated measurements.

characterized by the band structure and together with its complex refractive index, which are presented in Figs. 8(a) and 8(b), respectively. The real part of the refractive index represents the dispersion of the HHG in the medium, and the imaginary part represents the absorption of HHG. A field strength of 0.85 V/Å was used in the simulation, as it is close to the experimental estimate. Figures 8(c) and 8(d) show the simulation results, which clearly suggest that the HHSs are generated at the surface of the liquid flatjet (within 0.1 μm) and then propagate through 2 μm without intensity decrement, which are in good agreement with the experiment. It is worth noting that the spatial intensity profile of the focal spot was assumed to be a Gaussian distribution. The calculation was done by

$$S(\omega) = \frac{1}{\pi r_0^2} \int_0^{r_0} S_r(\omega) 2\pi r dr, \quad (1)$$

where the r_0 is the radius of the focal light spot and $S_r(\omega)$ is the spectral intensity at a distance r from the center of the focal light spot.

To investigate the yield difference between H_2O and CH_3CH_2OH, we simulated their HHG spectra based on two distinct band structures [Fig. 8(a)]. Our SBE calculations successfully reproduced the experimental results [see Fig. 8(f)], suggesting that the HHG spectra reflect the intrinsic properties of the liquids. This demonstrates that HHG can be utilized as a tool to probe the microscopic electronic structure of liquids.

VI. TIME-RESOLVED HHG MEASUREMENT

To investigate the ultrafast electron-driven dynamics in liquids via time-resolved HHSs, we integrated a pump–probe optical device into our liquid-phase HHG apparatus, as shown in Fig. 9(a). A fundamental NIR pulse (800 nm, 45 fs, 1 kHz) was divided by a beam splitter (BS, 70:30). The higher intensity portion served as the driving beam for HHG. The minor portion, serving as the pump pulse, was independently focused on the liquid jet in the second arm of the interferometer. The power of the two beams can be independently adjusted by rotating the half-wave plate (HWP) together using a linear polarizer (LP), ensuring that both beams are horizontally polarized. The time delay was controlled by a piezo-driven stick–slip motion stage from Nators (Model: LS-1730). Both beams are finally focused by passing through a plano-convex lens with a focusing length equals to 400 mm. Utilizing this configuration, we measured the time-resolved HHSs from liquid $(CH_3)_2CHOH$, shown in Figs. 9(b) and 9(c). The time delay between the pump and

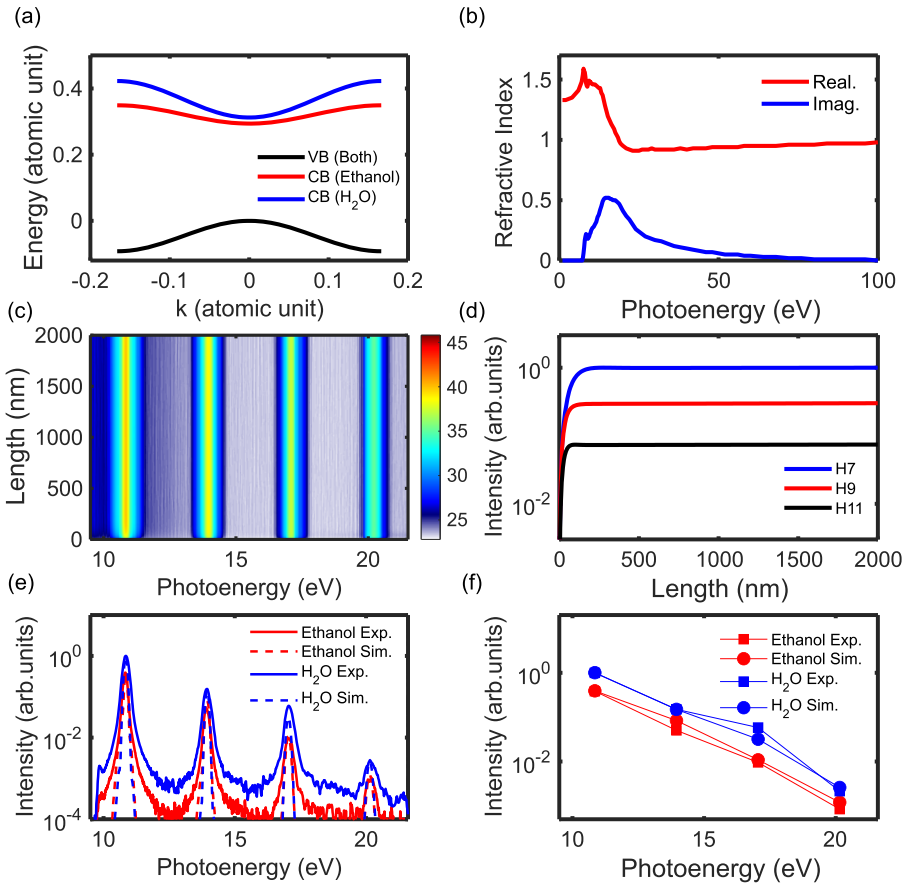

FIG. 8. Propagation effect and the influence of the band structure. (a) Band structure and (b) the complex refractive index[48] of H_2O. The H_2O's bandgap is 8 eV, and CH_3CH_2OH's bandgap is 8.5 eV.[49,50] (c) Simulated spectral intensity of H_2O concerning energy and propagation length; the displayed data are the logarithm of simulated spectral intensity. (d) H_2O's spectral intensity of H7, H9, and H11 through the flatjet was set 2 μm. (e) Comparison of the experiment data (shown by the solid line) and calculated data (shown by the dashed line). (f) Comparative experiments and calculations concerning the spectral intensity at specific harmonic orders.

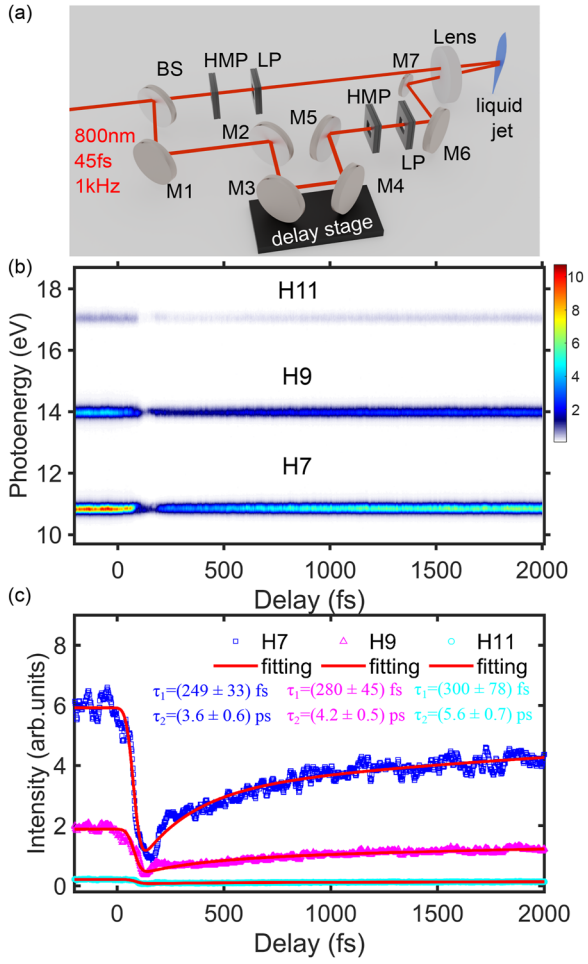

FIG. 9. Time-resolved HHG data of liquid $(CH_3)_2CHOH$. (a) Schematic representation of the pump–probe optical device. BS: beam splitter, M1–M7: reflective mirrors, HWP: half-wave plate, LP: linear polarizer, and lens: focusing lens. (b) 2D time-resolved HHS spectra of isopropanol. The positive delay signifies that the probe pulse follows the pump pulse. (c) 1D time-resolved HHSs for H7, H9, and H11 harmonics, obtained by integrating over all the time delays, are shown in (b).

probe pulses was scanned between −200 and +2000 fs in steps of 2 fs. The intensities of the pump and probe pulses were estimated to be 0.85 and 1.06 V/Å based on the focus spot size and the input power. At negative time delays, the pump pulse arrives after the probe, and the HHG intensity remains constant, demonstrating the high stability of the time-resolved measurement. The HHG intensity shows a significant depletion around time zero, where the pump and probe pulses temporally overlap. It begins to recover after a few hundred femtoseconds but remains weaker than its original level. These features serve as a distinct fingerprint of the early stages of electron relaxation dynamics. To deepen our understanding of the underlying dynamics, we analyzed the decay profile for each harmonic by a bi-exponential fitting equation,[51]

$$P(t) = I_0 + \left[\left(A_1 e^{-t/\tau_1} + A_2\left(1 - e^{-t/\tau_1}\right)e^{-t/\tau_2}\right) \times H(t)\right] \otimes G(t), \quad (2)$$

where I_0 represents the harmonic intensity without pumping. A_1 and A_2 are the amplitude factors of the two sequential decay processes, and τ_1 and τ_2 are their lifetimes, respectively. The lifetime τ_1 is the same as the rise time of τ_2. $H(t)$ is the Heaviside step function, and the cross-correlation function between the pump and probe pulses is given by $G(t)$, which was determined by the cross-correlation between two NIR pulses. The fitting results [red solid lines in Fig. 9(c)] accurately reproduce the experimental data, revealing a fast decay ranging from 249 fs to 300 fs and a slower process on the order of several ps. Having established the success of the semiconductor-like band structure model in describing the static harmonic spectrum (Sec. V), we now turn to elucidate the mechanism whereby a pump laser suppresses interband harmonic generation. This mechanism similarly explains the features observed in tr-HHG spectra of solids.[52–54] Following photo-excitation, the electron and hole become spatially displaced as the electric field drives them apart. Subsequent electron–hole scattering facilitates momentum and energy transfer, thereby depleting the spatial coherence of the pairs. This, in turn, leads to a suppression of coherent recombination. Consequently, the observed fast decay can be attributed to this scattering-induced dephasing. This observed electronic thermalization directly demonstrates the utility of tr-HHG for tracking ultrafast electron dynamics in liquids. On the other hand, it is known that substantial alterations to the electronic structure can significantly influence carrier dynamics and, consequently, also the HHG emission. However, excitation-induced dephasing primarily focuses on carrier interactions and does not consider significant reorganization of the material's electronic potential. The slower decay process shown in Fig. 9(c) signifies that electrons, upon excitation by pump light, attain a quasi-free state. This elevates the energies of the conduction bands above the Fermi energy level, representing an insulator-to-metal phase transition. Consequently, metallic free carriers lack the nonlinear response to the driving field required for generating high-harmonics, which is analogous to the slow decay processes observed in solids.[54,55] It is important to note that more sophisticated *ab initio* simulations, while beyond the scope of this study, are required to draw a definitive conclusion. Nevertheless, the stability and robustness of our experimental apparatus allow us to capture subtle changes in both static and time-dependent HHS from liquid samples. This capability promises to probe laser-induced modulations of electronic structure.

VII. CONCLUSION

A liquid-phase HHG apparatus has been constructed to investigate the ultrafast electron-driven processes associated with higher-order harmonics in liquids. The performance of this setup was examined using liquid $(CH_3)_2CHOH$, CH_3CH_2OH, and H_2O as samples, yielding their corresponding HHS. The HHS of all liquid samples exhibit four harmonics: H7, H9, H11, and H13, with harmonic intensity decreasing as its order increases. Furthermore, a pump–probe optical system is equipped into our liquid-phase HHG setup to access the time-resolved HHS measurement, enabling the

study of coherent electronic motions and bringing new possibilities toward the realm of attochemistry.[56–58]

ACKNOWLEDGMENTS

This work was supported by the National Natural Science Foundation of China (Grant Nos. 12474261 and 12450401) and the Synergic Extreme Condition User Facility (SECUF). Pengju Zhang acknowledges the support by Songshan Lake Materials Laboratory, Dongguan, Guangdong 523808, China (Grant No. 24D1201LS11). Tran Trung Luu acknowledges support from State Key Laboratory for Optical Quantum Materials and the fellowship of the IOP Center for International Collaboration.

AUTHOR DECLARATIONS

Conflict of Interest

The authors have no conflicts to disclose.

Author Contributions

Wenchao Zhao and Zepeng Qian contributed equally to this work.

Wenchao Zhao: Data curation (equal); Formal analysis (equal); Methodology (equal); Validation (equal); Writing – original draft (equal). **Zepeng Qian**: Data curation (equal); Formal analysis (equal); Software (equal); Writing – original draft (equal). **Yuanjie Pan**: Data curation (equal); Formal analysis (equal); Methodology (equal); Software (equal); Writing – original draft (equal). **Jinkai Zhang**: Methodology (supporting). **Menglong Zhao**: Methodology (supporting). **Gefei Li**: Methodology (supporting). **Tien-Dat Tran**: Software (supporting). **Tran Trung Luu**: Supervision (supporting). **Pengju Zhang**: Conceptualization (equal); Funding acquisition; Methodology (equal); Supervision (equal); Validation (equal).

DATA AVAILABILITY

Data underlying the results presented in this paper are not publicly available at this time but may be obtained from the authors upon reasonable request.

REFERENCES

[1] P. M. Paul, E. S. Toma, P. Breger, G. Mullot, F. Auge, P. Balcou, H. G. Muller, and P. Agostini, "Observation of a train of attosecond pulses from high harmonic generation," Science **292**, 1689–1692 (2001).
[2] M. Hentschel, R. Kienberger, C. Spielmann, G. A. Reider, N. Milosevic, T. Brabec, P. Corkum, U. Heinzmann, M. Drescher, and F. Krausz, "Attosecond metrology," Nature **414**, 509–513 (2001).
[3] M. Isinger, R. J. Squibb, D. Busto, S. Zhong, A. Harth, D. Kroon, S. Nandi, C. L. Arnold, M. Miranda, J. M. Dahlström, E. Lindroth, R. Feifel, M. Gisselbrecht, and A. L'Huillier, "Photoionization in the time and frequency domain," Science **358**, 893–896 (2017).
[4] G. Schmid, K. Schnorr, S. Augustin, S. Meister, H. Lindenblatt, F. Trost, Y. Liu, N. Stojanovic, A. Al-Shemmary, T. Golz, R. Treusch, M. Gensch, M. Kübel, L. Foucar, A. Rudenko, J. Ullrich, C. D. Schröter, T. Pfeifer, and R. Moshammer, "Terahertz-field-induced time shifts in atomic photoemission," Phys. Rev. Lett. **122**, 073001 (2019).
[5] M. Huppert, I. Jordan, D. Baykusheva, A. von Conta, and H. J. Wörner, "Attosecond delays in molecular photoionization," Phys. Rev. Lett. **117**, 093001 (2016).
[6] X. Gong, S. Heck, D. Jelovina, C. Perry, K. Zinchenko, R. Lucchese, and H. J. Wörner, "Attosecond spectroscopy of size-resolved water clusters," Nature **609**, 507–511 (2022).
[7] S. Heck, M. Han, D. Jelovina, J.-B. Ji, C. Perry, X. Gong, R. Lucchese, K. Ueda, and H. J. Wörner, "Two-center interference in the photoionization delays of Kr_2," Phys. Rev. Lett. **129**, 133002 (2022).
[8] I. Jordan, M. Huppert, D. Rattenbacher, M. Peper, D. Jelovina, C. Perry, A. von Conta, A. Schild, and H. J. Wörner, "Attosecond spectroscopy of liquid water," Science **369**, 974–979 (2020).
[9] S. Neppl, R. Ernstorfer, E. M. Bothschafter, A. L. Cavalieri, D. Menzel, J. V. Barth, F. Krausz, R. Kienberger, and P. Feulner, "Attosecond time-resolved photoemission from core and valence states of magnesium," Phys. Rev. Lett. **109**, 087401 (2012).
[10] M. Volkov, S. A. Sato, F. Schlaepfer, L. Kasmi, N. Hartmann, M. Lucchini, L. Gallmann, A. Rubio, and U. Keller, "Attosecond screening dynamics mediated by electron localization in transition metals," Nat. Phys. **15**, 1145–1149 (2019).
[11] A. McPherson, G. Gibson, H. Jara, U. Johann, T. S. Luk, I. A. McIntyre, K. Boyer, and C. K. Rhodes, "Studies of multiphoton production of vacuum-ultraviolet radiation in the rare gases," J. Opt. Soc. Am. B **4**, 595–601 (1987).
[12] G. Vampa, T. J. Hammond, N. Thiré, B. E. Schmidt, F. Légaré, C. R. McDonald, T. Brabec, and P. B. Corkum, "Linking high harmonics from gases and solids," Nature **522**, 462–464 (2015).
[13] P. B. Corkum, "Plasma perspective on strong field multiphoton ionization," Phys. Rev. Lett. **71**, 1994–1997 (1993).
[14] A. H. Chin, O. G. Calderón, and J. Kono, "Extreme midinfrared nonlinear optics in semiconductors," Phys. Rev. Lett. **86**, 3292–3295 (2001).
[15] S. Ghimire, A. D. DiChiara, E. Sistrunk, P. Agostini, L. F. DiMauro, and D. A. Reis, "Observation of high-order harmonic generation in a bulk crystal," Nat. Phys. **7**, 138–141 (2011).
[16] T. T. Luu, M. Garg, S. Y. Kruchinin, A. Moulet, M. T. Hassan, and E. Goulielmakis, "Extreme ultraviolet high-harmonic spectroscopy of solids," Nature **521**, 498–502 (2015).
[17] E. Goulielmakis and T. Brabec, "High harmonic generation in condensed matter," Nat. Photonics **16**, 411–421 (2022).
[18] C. Heide, Y. Kobayashi, S. R. U. Haque, and S. Ghimire, "Ultrafast high-harmonic spectroscopy of solids," Nat. Phys. **20**, 1546–1557 (2024).
[19] S. M. Cavaletto, K. M. Kowalczyk, F. O. Navarrete, and J. Rivera-Dean, "The attoscience of strong-field-driven solids," Nat. Rev. Phys. **7**, 38–49 (2024).
[20] A. Flettner, T. Pfeifer, D. Walter, C. Winterfeldt, C. Spielmann, and G. Gerber, "High-harmonic generation and plasma radiation from water microdroplets," Appl. Phys. B **77**, 747–751 (2003).
[21] H. G. Kurz, D. S. Steingrube, D. Ristau, M. Lein, U. Morgner, and M. Kovačev, "High-order-harmonic generation from dense water microdroplets," Phys. Rev. A. **87**, 063811 (2013).
[22] H. G. Kurz, M. Kretschmar, T. Binhammer, T. Nagy, D. Ristau, M. Lein, U. Morgner, and M. Kovačev, "Revealing the microscopic real-space excursion of a laser-driven electron," Phys. Rev. X **6**, 031029 (2016).
[23] M. J. Tauber, R. A. Mathies, X. Chen, and S. E. Bradforth, "Flowing liquid sample jet for resonance Raman and ultrafast optical spectroscopy," Rev. Sci. Instrum. **74**, 4958–4960 (2003).
[24] A. D. DiChiara, E. Sistrunk, T. A. Miller, P. Agostini, and L. F. DiMauro, "An investigation of harmonic generation in liquid media with a mid-infrared laser," Opt. Express **17**, 20959–20965 (2009).
[25] M. Kondoh and M. Tsubouchi, "Liquid-sheet jets for terahertz spectroscopy," Opt. Express **22**, 14135–14147 (2014).
[26] M. Ekimova, W. Quevedo, M. Faubel, P. Wernet, and E. T. J. Nibbering, "A liquid flatjet system for solution phase soft-x-ray spectroscopy," Struct. Dyn. **2**, 054301 (2015).
[27] G. Galinis, J. Strucka, J. C. T. Barnard, A. Braun, R. A. Smith, and J. P. Marangos, "Micrometer-thickness liquid sheet jets flowing in vacuum," Rev. Sci. Instrum. **88**, 083117 (2017).

[28]J. D. Koralek, J. B. Kim, P. Brůža, C. B. Curry, Z. Chen, H. A. Bechtel, A. A. Cordones, P. Sperling, S. Toleikis, J. F. Kern *et al.*, "Generation and characterization of ultrathin free-flowing liquid sheets," Nat. Commun. **9**, 1353 (2018).
[29]J. C. T. Barnard, J. P. Lee, O. Alexander, S. Jarosch, D. Garratt, R. Picciuto, K. Kowalczyk, C. Ferchaud, A. Gregory, M. Matthews, and J. P. Marangos, "Delivery of stable ultra-thin liquid sheets in vacuum for biochemical spectroscopy," Front. Mol. Biosci. **9**, 1044610 (2022).
[30]Y.-P. Chang, Z. Yin, T. Balciunas, H. J. Wörner, and J.-P. Wolf, "Temperature measurements of liquid flat jets in vacuum," Struct. Dyn. **9**, 014901 (2022).
[31]T. Gallo, L. Adriano, M. Heymann, A. Wrona, N. Walsh, G. Öhrwall, F. Callefo, S. Skruszewicz, M. Namboodiri, R. Marinho, J. Schulz, and J. Valerio, "Development of a flat jet delivery system for soft x-ray spectroscopy at max iv," J. Synchrotron Radiat. **31**, 1285–1292 (2024).
[32]R. Gnewkow, H. Stiel, A. Jonas, S. Schönfelder, J. Probst, T. Krist, B. Kangiesser, and I. Mantouvalou, "Laboratory soft x-ray setup for transient absorption experiments in the liquid phase using a laser-produced plasma source," Optica **11**, 744–752 (2024).
[33]T. T. Luu, Z. Yin, A. Jain, T. Gaumnitz, Y. Pertot, J. Ma, and H. J. Wörner, "Extreme–ultraviolet high–harmonic generation in liquids," Nat. Commun. **9**, 3723 (2018).
[34]Z. Yin, T. T. Luu, and H. J. Wörner, "Few-cycle high-harmonic generation in liquids: In-operando thickness measurement of flat microjets," J. Phys.: Photonics **2**, 044007 (2020).
[35]A.-W. Zeng and X.-B. Bian, "Impact of statistical fluctuations on high harmonic generation in liquids," Phys. Rev. Lett. **124**, 203901 (2020).
[36]V. Svoboda, Z. Yin, T. T. Luu, and H. J. Wörner, "Polarization measurements of deep- to extreme-ultraviolet high harmonics generated in liquid flat sheets," Opt. Express **29**, 30799–30808 (2021).
[37]O. Neufeld, Z. Nourbakhsh, N. Tancogne-Dejean, and A. Rubio, "*Ab initio* cluster approach for high harmonic generation in liquids," J. Chem. Theor. Comput. **18**, 4117–4126 (2022).
[38]A. Mondal, O. Neufeld, Z. Yin, Z. Nourbakhsh, V. Svoboda, A. Rubio, N. Tancogne-Dejean, and H. J. Wörner, "High-harmonic spectroscopy of low-energy electron-scattering dynamics in liquids," Nat. Phys. **19**, 1813–1820 (2023).
[39]A. Mondal, B. Waser, T. Balciunas, O. Neufeld, Z. Yin, N. Tancogne-Dejean, A. Rubio, and H. J. Wörner, "High-harmonic generation in liquids with few-cycle pulses: Effect of laser-pulse duration on the cut-off energy," Opt. Express **31**, 34348–34361 (2023).
[40]Y. H. Kim, H. Kim, S. C. Park, Y. Kwon, K. Yeom, W. Cho, T. Kwon, H. Yun, J. H. Sung, S. K. Lee *et al.*, "High-harmonic generation from a flat liquid-sheet plasma mirror," Nat. Commun. **14**, 2328 (2023).
[41]O. Alexander, J. C. T. Barnard, E. W. Larsen, T. Avni, S. Jarosch, C. Ferchaud, A. Gregory, S. Parker, G. Galinis, A. Tofful, D. Garratt, M. R. Matthews, and J. P. Marangos, "Observation of recollision-based high-harmonic generation in liquid isopropanol and the role of electron scattering," Phys. Rev. Res. **5**, 043030 (2023).
[42]T. Yang, T. Kurihara, Y. Hua, T. Mizuno, T. Kanai, S. Ashihara, Y. Harada, and J. Itatani, "Enhancement of high harmonic generation in liquid water by resonant excitation in the mid-infrared," APEX **17**, 122006 (2024).
[43]J. Xu and S. Meng, "High-harmonic generation and femtosecond-resolved ultrafast dynamics in liquid water," J. Phys. Chem. Lett. **16**, 5295–5301 (2025).
[44]A. Cavagna, M. Eder, E. Chowdhury, A. Kalouguine, J. Kaur, G. Mourou, S. Haessler, and R. Lopez-Martens, "Continuous relativistic high-harmonic generation from a kHz liquid-sheet plasma mirror," Opt. Lett. **50**, 165–168 (2025).
[45]Z. Yin, Y.-P. Chang, T. Balčiūnas, Y. Shakya, A. Djorović, G. Gaulier, G. Fazio, R. Santra, L. Inhester, J.-P. Wolf, and H. J. Wörner, "Femtosecond proton transfer in urea solutions probed by x-ray spectroscopy," Nature **619**, 749–754 (2023).
[46]Y.-P. Chang, T. Balciunas, Z. Yin, M. Sapunar, B. N. C. Tenorio, A. C. Paul, S. Tsuru, H. Koch, J.-P. Wolf, S. Coriani, and H. J. Wörner, "Electronic dynamics created at conical intersections and its dephasing in aqueous solution," Nat. Phys. **21**, 137–145 (2025).
[47]A. Mondal, O. Neufeld, T. Balciunas, B. Waser, S. Müller, M. Rossi, Z. Yin, A. Rubio, N. Tancogne-Dejean, and H. J. Wörner, "Multi-plateau high-harmonic generation in liquids driven by off-site recombination," Nat. Photon. (published online 2025).
[48]H. Hayashi and N. Hiraoka, "Accurate measurements of dielectric and optical functions of liquid water and liquid benzene in the VUV region (1–100 eV) using small-angle inelastic x-ray scattering," J. Phys. Chem. B **119**, 5609–5623 (2015).
[49]S. Schreck, A. Pietzsch, K. Kunnus, B. Kennedy, W. Quevedo, P. S. Miedema, P. Wernet, and A. Föhlisch, "Dynamics of the oh group and the electronic structure of liquid alcohols," Struct. Dyn. **1**, 054901 (2014).
[50]Z. Yin, I. Rajkovic, S. Thekku Veedu, S. Deinert, D. Raiser, R. Jain, H. Fukuzawa, S.-i. Wada, W. Quevedo, B. Kennedy, S. Schreck, A. Pietzsch, P. Wernet, K. Ueda, A. Föhlisch, and S. Techert, "Ionic solutions probed by resonant inelastic x-ray scattering," Z. Phys. Chem. **229**, 1855–1867 (2015).
[51]S. Karashima, Y.-I. Suzuki, and T. Suzuki, "Ultrafast extreme ultraviolet photoelectron spectroscopy of nonadiabatic photodissociation of CS_2 from $^1B_2$ ($1\Sigma_u^+$) state: Product formation via an intermediate electronic state," J. Phys. Chem. Lett. **12**, 3755–3761 (2021).
[52]Z. Wang, H. Park, Y. H. Lai, J. Xu, C. I. Blaga, F. Yang, P. Agostini, and L. F. DiMauro, "The roles of photo-carrier doping and driving wavelength in high harmonic generation from a semiconductor," Nat. Commun. **8**, 1686 (2017).
[53]M. R. Bionta, E. Haddad, A. Leblanc, V. Gruson, P. Lassonde, H. Ibrahim, J. Chaillou, N. Émond, M. R. Otto, Á. Jiménez-Galán, R. E. F. Silva, M. Ivanov, B. J. Siwick, M. Chaker, and F. Légaré, "Tracking ultrafast solid-state dynamics using high harmonic spectroscopy," Phys. Rev. Res. **3**, 023250 (2021).
[54]Y. Wang, J. Gao, Y. Liu, P. Jiang, J. Xiao, Z. Zhou, H. Yang, G. Lu, L.-Y. Peng, Y. Liu, Q. Gong, and C. Wu, "All-optical control of high-order harmonic generation in correlated systems," Photonics Res. **12**, 2831 (2024).
[55]P. J. van Essen, Z. Nie, B. de Keijzer, and P. M. Kraus, "Toward complete all-optical intensity modulation of high-harmonic generation from solids," ACS Photonics **11**, 1832–1843 (2024).
[56]H. J. Wörner, C. A. Arrell, N. Banerji, A. Cannizzo, M. Chergui, A. K. Das, P. Hamm, U. Keller, P. M. Kraus, E. Liberatore *et al.*, "Charge migration and charge transfer in molecular systems," Struct. Dyn. **4**, 061508 (2017).
[57]I. C. D. Merritt, D. Jacquemin, and M. Vacher, "Attochemistry: Is controlling electrons the future of photochemistry?," J. Phys. Chem. Lett. **12**, 8404–8415 (2021).
[58]F. Martín, F. Calegari, C. Vozzi, K. Ueda, and L. DiMauro, "Virtual special issue on attosecond chemistry," J. Phys. Chem. A **128**, 4761–4764 (2024).